C. Alberto Sánchez-Delgado
Universidad Autónoma del Estado de México,
Instituto Literario 100, col. Centro,
50000, Toluca, México
e-mail: csanchezd005@alumno.uaemex.mx

Juan Carlos Ávila Vilchis[1]
Universidad Autónoma del Estado de México,
Instituto Literario 100, col. Centro,
50000, Toluca, México
e-mail: jcavilav@uaemex.mx

Adriana H. Vilchis-González
Universidad Autónoma del Estado de México,
Instituto Literario 100, col. Centro,
50000, Toluca, México
e-mail: avilchisg@uaemex.mx

Belem Saldivar
Universidad Autónoma del Estado de México,
Instituto Literario 100, col. Centro,
50000, Toluca, México;
Cátedras CONACYT,
Av. Insurgentes Sur 1582,
Col. Crédito Constructor,
Alcaldía Benito Juárez,
03940, Ciudad de México, México
e-mail: mbsaldivarma@conacyt.mx

Nonlinear Oscillator-Based Gait Generation for a Novel Aero-Terrestrial Bioinspired Robotic System

This paper focuses on the design of a novel aero-terrestrial robotic system based on the morphology of the Hymenoptera order insects and, particularly, on a strategy based on nonlinear oscillators for the coordination of its 12 terrestrial degrees-of-freedom (DoF). The ability of this new aero-terrestrial robot to, successfully, perform the walking process is validated through numerical simulations and tests performed on an experimental platform in which the gait speed was varied from 0.04 to 0.2 m/s. Some of the most important qualities of this robotic system are a relatively simple design with only 2 DoF per leg and a versatile terrestrial locomotion with the ability to vary its speed and direction in real-time with smooth transitions. Furthermore, unlike existent similar systems, the robot is designed to initiate a flight phase in any position without adopting particular postures avoiding undesirable interferences with the walking configuration.
[DOI: 10.1115/1.4047269]

1 Introduction

The research effort on versatility improvement over the mobility of robots has led to the integration of several modes of locomotion (terrestrial, aerial, or aquatic) into a single system. The development of designs and algorithms that control and link modes of locomotion is a research area of growing interest [1,2]. In both animals and mobile robots, locomotion is a fundamental activity for the tasks development. The ability to move through an environment empowers the systems for undertaking activities such as navigation or cooperation. An important branch in mobile robotics research is devoted to the development of systems capable of moving despite physical barriers. The success in this depends on the physical capabilities of the robot and on the strategies proposed to evade obstacles. A robot with a mono-modal locomotion will find the navigation task more difficult than a robot with several modes [1,2].

Insects have the virtues of multimodal locomotion in the development of complex tasks. Hymenoptera insects excel by the use of their locomotive capabilities in complex tasks such as construction, collection, and cooperation. These tasks are not trivial in robotics research and represent challenges as coordination or aero-terrestrial tracking, for instance. Therefore, the study and mimicry of biological mechanisms could promote advances in the field of locomotion and robotic navigation [3].

Integrating several modes of locomotion into a single system faces some difficulties such as the weight and complexity increase. In Ref. [4], some paradigms are introduced to address these problems in three ways: (a) the additive approach in which each locomotion mode uses a greater number of mechanisms and actuators, (b) the semi-additive approach in which the same actuators are used for different mechanisms, and (c) the integrative approach where the same actuators and mechanisms are used in different modes, decreasing performance and versatility due to a reduced number of DoF.

Currently, there are several proposals regarding the integration of land and aerial modes of locomotion into a single robotic system. Based on morphology aspects, robots can be grouped into three categories:

(1) *The union of a ground rolling structure and a flight system.* In Ref. [5], the Deployable Air-Land Exploration Robot system is designed under the integrative approach. It consists of an airplane structure that accomplishes the aerial mode of locomotion while on the ground uses its wings as rims to move.

The aerial/terrestrial robot system [6] uses a semi-additive approach and consists of a quadcopter attached to an exoskeleton by means of an axis around which it can rotate freely, generating a thrust force that allows it to roll on the ground.

(2) *The union of a multicopter and a legged walker.* In nature, locomotion by legs is extensively used even in animals with the ability to fly (see Refs. [7–12]). A semi-additive proposal is presented in Ref. [7] where, for walking on inclined surfaces, the system descends due to the gravity effect. To climb slopes, the device uses the thrust force of the propellers as an impulse. The flying monkey [8] is an eight-legged quadcopter based on an origami-inspired folding mechanism developed under an integrative paradigm. Although its legs limit its mobility to one-degree-of-freedom, the system is able to turn thanks to the yaw force produced by the rotors. The walking quadcopter proposed in Ref. [9], under an integrative approach, employs crawling legs for terrestrial locomotion. Each of its legs consists of a four-bars-sliding-crank mechanism, which, subjected to a crushing force provided by the propellers, elongates to achieve displacement. The legs return to their original configuration when the crushing force disappears. Another system suggests the addition of an 18 DoF-hexapod with a multicopter as the robot in

Ref. [10] that attaches a propeller to each femoral segment to provide aerial locomotion. Another robot described in Refs. [11,12] uses four propellers coupled to the corner legs. In both cases, it is necessary for the robot to adopt a predetermined posture to start the flight, restricting legs mobility.

(3) *The union of terrestrial locomotion and folding wings.* The ornithopter [13] is a bipedal robot under the semi-additive approach with flapping wings. It is able to activate both the wings and the legs to navigate through complex three-dimensional terrains with a single motor. For the transition between gait and flight, it must run to get enough aerodynamic momentum to take off. Inspired by bats, the MultiMo-Bat [14] is able to glide and perform jumps. The locomotion takes place in three phases. First, a gearmotor is activated to fold the legs and store energy in springs. Second, this energy is released pushing the robot to jump. Finally, at maximum altitude, the robot opens its wings to glide until its landing.

The aforementioned systems combine aerial with terrestrial locomotion. Both types of locomotion deserve robust and detailed discussions. Nevertheless, this paper focuses on the terrestrial locomotion of an aero-terrestrial bioinspired robot and addresses its mechanical system, its electronic interface, and its gait generation part.

Locomotion by legs has advantages over other types of terrestrial locomotion (e.g., wheels or caterpillar tracks) as the ability to cross uneven terrains with obstacles [15]. However, this implies an increment in mechanical complexity that could demand sophisticated control strategies [1,16].

One challenge in legged locomotion is the coordination of several DoF to achieve a desired displacement. The inverse kinematic approach and the use of predetermined movements have been applied on the development of legged robots. Nonetheless, conventional approaches have disadvantages such as requiring a mathematical model, continuous calculation of trajectories, or low robustness with respect to external disturbances [17,18].

In nature, central pattern generators (CPGs) are neural circuits that produce rhythmic impulse patterns without feedback. These systems are connected in networks to control processes such as breathing, heart rhythm, or limb coordination [19,20]. Artificial CPGs are bioinspired alternatives for the generation of cyclic movements as in gait processes. In robotics research, CPGs are produced by connectionist models, vector maps, or coupled oscillator systems [21] to be applied in swimming robots [22], walking robots [23,24], manipulators [25–27], or prosthetics [28]. Concerning walking bioinspired robots, the authors in Ref. [29] propose a neural circuit-based approach to control, in an adaptive way, a hexapod evolving in an unstructured environment. Results of this work prove that a single CPG control enables self-adaptation by using chaotic dynamics and synaptic plasticity.

Most of the research in this area focuses on the integration of physical structures from a design perspective without, explicitly, considering locomotion control strategies [5,7,9,11,13,14].

In this paper, a novel aero-terrestrial robot with propellers based on Hymenoptera morphology and locomotion is presented. A linkage mechanism implemented in its legs allows reducing the number of actuators from 18, as in most of the reported works, to 12. This mechanism helps the propellers to always keep parallelism with the ground during land locomotion giving the system the capability of flying from any gait configuration. This is a new advantage since previous works need to change their configuration to start the flying mode.

This paper is organized as follows. Section 2 focuses on a description of the system mechanical structure and electronic architecture. Section 3 introduces the use of nonlinear oscillators for gait generation. Section 4 provides a set of oscillators-based numerical simulations. Section 5 reports experimental results. Specific aspects of this work are discussed in Sec. 6. Concluding remarks and future work are presented at the end of this paper.

2 System Description

Bio-inspiration overview. As mentioned in Sec. 1, Hymenoptera stands out for their locomotion capabilities in complex environments. Its morphology, its integration of flight and walking, the way in which they coordinate their movements, and the oscillatory nature of their nerve control centers are fundamental for their high performance. These characteristics constitute the bio-inspiration for the design of the robot presented in this investigation.

2.1 Mechanical Structure.
The robotic system proposed in this paper looks for keeping the original structure of Hymenoptera in the sense of considering a segmented body in three parts (head, abdomen, and thorax), having six articulated legs and integrating, in a single system, structures necessary for flight and walking. The legs of the system are composed of three segments. Starting from the proximal to the distal extremes, these segments are coxa, femur, and tibia resembling Hymenoptera legs, as it is illustrated in Fig. 1.

The coxa attaches the leg with the body. The femur is a four-bar mechanism highlighted, with the dashed lines, in Fig. 1. The tibia is the leg end-effector. These segments are linked by the thorax-coxa (TC), the coxa-trochanterofemur (CTr), and the femur-tibia (FT) joints. Servomotors actuate the first two joints, while FT joints are passive (see Fig. 1).

The servomotor characteristics are a weight of 0.539 N, dimensions of 0.0407 m × 0.0197 m × 0.0429 m, a stall torque of 0.9218 Nm, a stall current of 2.5 A at 6 V, and a frequency of 50 Hz. The leg segments were manufactured in polylactic acid (PLA) using a 3D printer.

The coxa, coupled to a servomotor, is a C-shaped structure capable of rotating with respect to the TC axis (see Fig. 1). The femur consists of a four-bar linkage, which always maintain parallelism. The tibia is an extension of this mechanism having at its distal part a semicircular element substituting the tarsus, giving support to the entire leg.

The body of the robot resembles the Hymenoptera structure where the abdomen, thorax, and head are identified in Fig. 2. The abdomen and the thorax are composed of plates supporting electronic elements as control cards, electronic speed controller (ESC), and battery. The head contains a pair of servomotors and a camera. As for the legs, part of the body was manufactured in PLA.

Figure 3 shows the assembled hexapod with its legs attached to the body and holding propellers, control cards, and battery. The propellers are mounted in the highest part of the tibia, near FT joints. Due to the four-bar mechanism, the propellers always remain parallel to the ground, regardless of the movements made by the leg. This would give the system the ability to freely move its lower appendices during flight, as in the case of Hymenoptera, increasing its
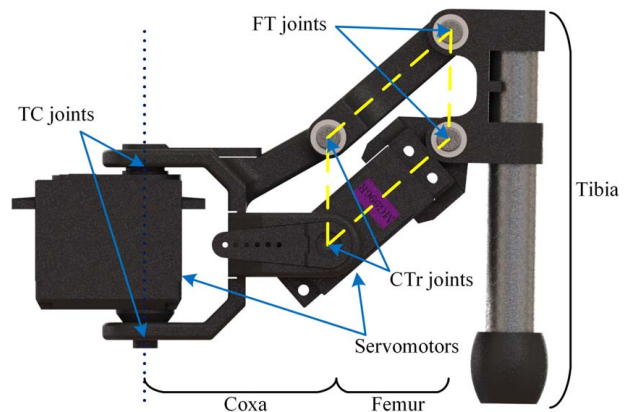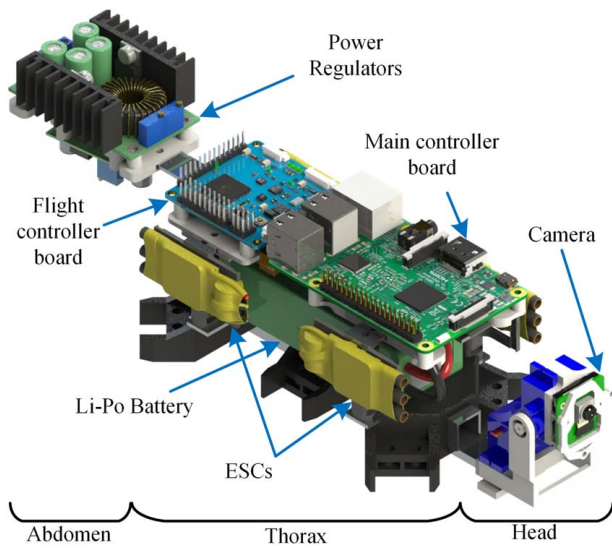

Fig. 1 Hexapod leg detail

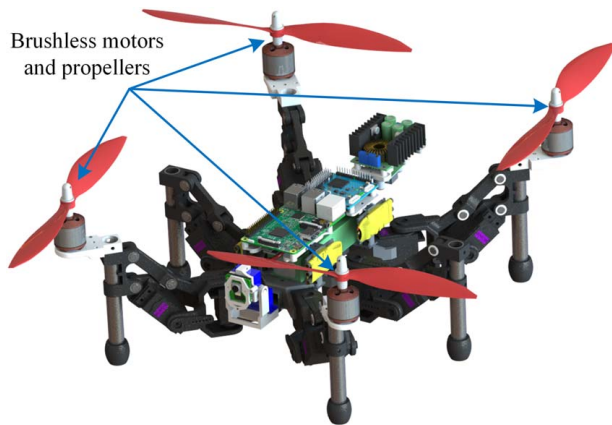**Fig. 2   Body of the bioinspired robotic system**

Fig. 3   Complete view of the proposed system

versatility with respect to other devices, which must maintain a rigid attitude while flying (see Refs. [10,11]).

2.2   Electronic Architecture. An electronic system is proposed to drive the aerial and terrestrial modes of locomotion of the robot. Figure 4 shows a diagram of the electronic architecture, where blocks represent elements and arrows are signals.

The angular position of the servomotors is controlled by a PCA9685 pulse width modulated (PWM) generator circuit, which is connected, via an inter-integrated circuit (I2C) interface, to the main controller board running a CPG network. Four brushless motors will be commanded through ESC by a Crius v2.6 flight controller board that will communicate with the mainboard via an FT232 converter.

The flight controller board will receive activation commands and requests of three embedded sensors (accelerometer, barometer, and magnetometer). A pair of optical proximity sensors GP2Y0E03 is used to acquire the distances from the robot to the ground and to a frontal obstacle.

An eight-megapixel Pi camera connected by its own bus to the mainboard is available for future research on artificial vision-based navigation. The mainboard, a Raspberry Pi model 3 b+, is responsible for leg coordination algorithms, sensors monitoring, the transition between flight and gait, remote communication, and camera management. These functions are mounted on the robotic operating system (ROS) in order to establish distributed processing and communication with a remote computer through a Wi-Fi network [30].

A three-cell lithium-polymer (Li-Po) battery is used as a power source. In order to provide adequate voltage and current levels to the electronics, two commutated regulators are implemented. The first regulator provides 5 V at 3 A for the main control board and sensors, while the second one provides 6 V at 12 A to the servomotors. Electric current flows from the battery through each of the ESC to the respective brushless motor.

The union of the mechanical structure with the electronic architecture generates an experimental platform (EP) that is used to perform the experimental tests reported in Sec. 5.

3   Models for Gait Generation

In Hymenoptera and insects in general, the walking pattern is a consequence of the synchronization between nerve control centers that generate cyclic signals. The oscillatory characteristics of
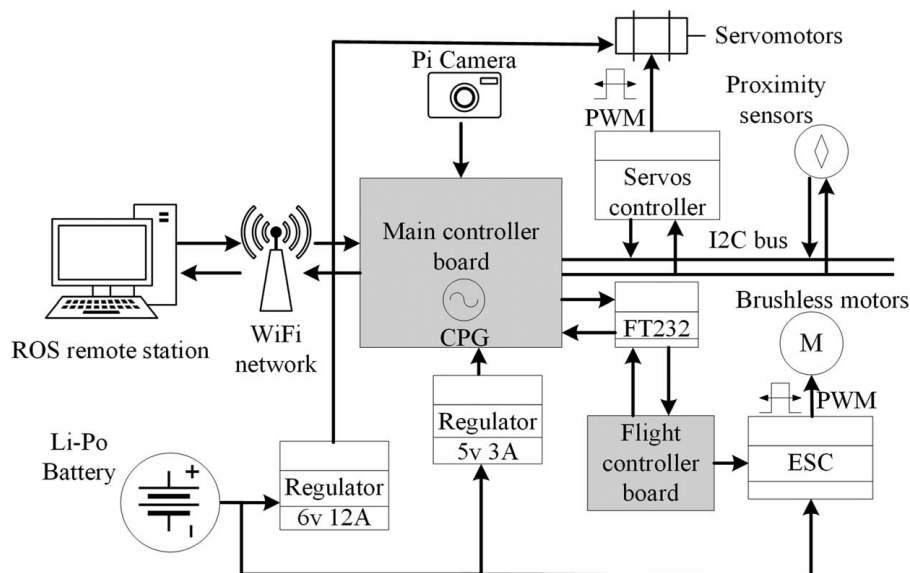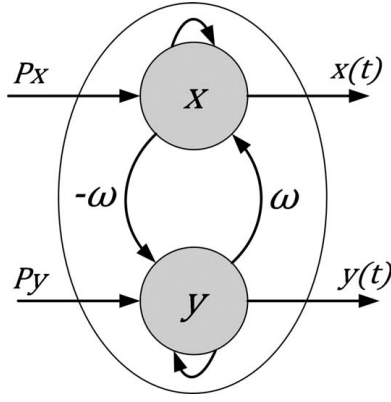

Fig. 4   Proposed electronic architecture

Fig. 5 Hopf oscillator as a pair of coupled neurons

Fig. 7 Time response of a single Hopf oscillator

these centers, as well as their ability to be modulated, have been taken as the basis of bio-inspiration for the development of the algorithms that govern the robot gait reported in this paper.

This section describes the Hopf oscillator and the Hopf oscillator-based CPG network used to drive the gait process of the proposed robotic system for both numerical simulations and experiments.

3.1 Hopf Oscillator Model. As mentioned before, walking is a cyclic process that can be described and recreated artificially by oscillators. To avoid gait limitations, the oscillator that describes the walking must have adjustable parameters (frequency, amplitude, and phase) and be robust against external disturbances.

There are several models that satisfy the described requirements such as the Van der Pol or the Rayleigh nonlinear oscillators. However, the Hopf oscillator stands out for presenting parameters clearly related to its harmonic output, for being a widely studied model and for its simplicity [31,32]. The dynamic behavior of the Hopf oscillator can be described in a polar form or in its respective cartesian representation as in Eq. (1):

$$
\begin{aligned}
\dot{x}(t) &= \alpha[\mu - x^2(t) - y^2(t)]x(t) + \omega y(t) + P_x \\
\dot{y}(t) &= \alpha[\mu - x^2(t) - y^2(t)]y(t) - \omega x(t) + P_y
\end{aligned}
\tag{1}
$$

where $x(t)$ and $y(t)$ represent the states of the oscillator whose units are deg, $\dot{x}(t)$ and $\dot{y}(t)$ are their first-order time derivatives, ω its frequency in Hz, μ is a parameter that determines the stability of the
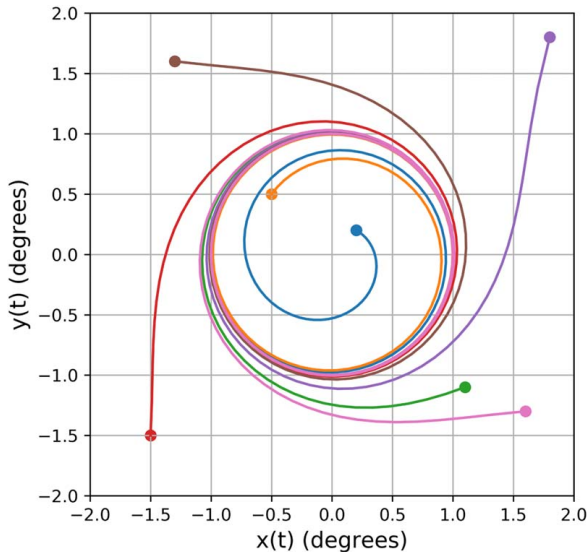

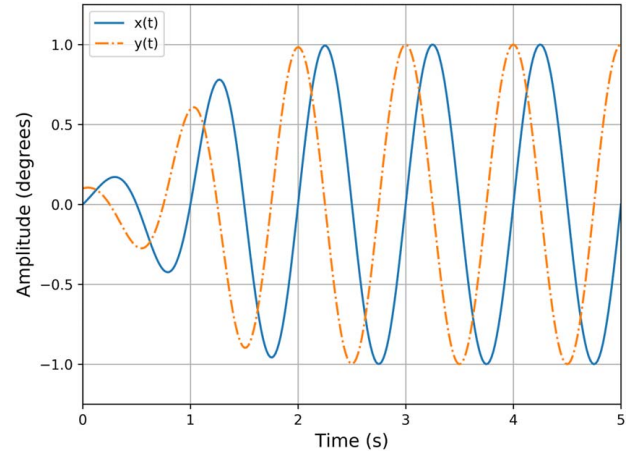**Fig. 6 Limit cycle of a single Hopf oscillator**

oscillation in deg^2, P_x and P_y are external perturbation in deg/s, and α is a convergence speed parameter in deg^{-2}s^{-1}. The amplitudes of the oscillators are related through a transformation from the CPG-output space to the articular space.

Under a biological perspective, a CPG is composed of a pair of neurons coupled through inhibitory and excitatory connections, which, together, produce alternating rhythmic activity. This description allows introducing a simplified representation based on the states of the Hopf oscillator as shown in Fig. 5.

Stable limit cycles are a primary feature of the oscillators. Figure 6 shows the limit cycle of a single Hopf oscillator with the parameters $\mu = 1$, $\omega = 2\pi$, and $\alpha = 2$, where the dots represent different initial conditions. It is observed that all trajectories converge to the limit cycle defined as $x(t)^2 + y(t)^2 = \mu$.

Under the parameters previously used, Fig. 7 shows the states behaviors with initial conditions $x(0) = 0$ and $y(0) = 0.1$. As it can be observed, the states reach the same amplitude value in the stationary regime with a phase angle $\eta = 90$ deg. This is an inherent characteristic of the Hopf oscillator.

3.2 Central Pattern Generator as a Network of Coupled Nonlinear Hopf Oscillators. A single oscillator is capable of directing the cyclic movement of one joint regardless the remaining joints status. However, it does not allow the generation of the walking pattern. It is well known that coupled limit-cycle oscillators are often used to describe and analyze synchronization and pattern formations [33].

In this paper, to generate a walking pattern for the 12 terrestrial DoF robot, an array of coupled Hopf oscillator network-based CPG is proposed. In order to generate a coordinated walking, the dynamics of each oscillator must consider external perturbations and the current states of the other oscillators. This condition is achieved by coupling the oscillators in such a way that the outputs of an oscillator represent an external disturbance for an adjacent oscillator. Figure 8 illustrates two coupled oscillators.

Unlike a single Hopf oscillator that undergoes dynamics on a limit cycle, in coupled Hopf oscillators, "the phases can lock, and phase patterns can form" [33]. In Ref. [33], the authors explore the deterministic pattern formation for a two-dimensional array of identical Hopf oscillators, and simulations reveal various stationary and non-stationary patterns in different parameter regimes. These patterns determine the phase synchronization dynamics of limit-cycle oscillators.

Equation (2) describes the coupling between oscillators i and j [34]:

$$
\begin{bmatrix} \dot{x}_i \\ \dot{y}_i \end{bmatrix} = \begin{bmatrix} \alpha(\mu_i - r_i^2) & -\omega \\ \omega & \alpha(\mu_i - r_i^2) \end{bmatrix} \begin{bmatrix} x_i \\ y_i \end{bmatrix} + \varepsilon \sum_{j \neq i} C(\theta_{ij}) \begin{bmatrix} x_j \\ y_j \end{bmatrix}
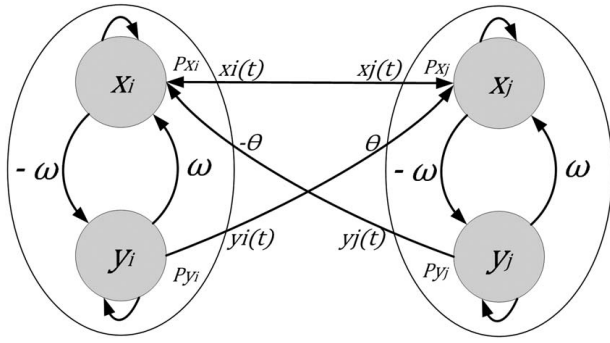\tag{2}
$$

Fig. 8 Coupling between oscillators

In Eq. (2), θ_{ij} is the desired relative phase between the i and j oscillators that keeps the relation $\theta_{ij} = -\theta_{ji}$, ε is a parameter determining the coupling strength between oscillators that has been heuristically adjusted, and $C(\theta_{ij})$ is a coupling matrix defined by Eq. (3):

$$C(\theta_{ij}) = \begin{bmatrix} \cos \theta_{ij} & -\sin \theta_{ij} \\ 0 & 0 \end{bmatrix} \qquad (3)$$

As stated previously, terrestrial locomotion has been inspired by Hymenoptera. Taking the ants as a reference, the tripod walking pattern (three legs are always in contact with the ground) prevails over other patterns regardless the change in speed, trajectory, or load. In addition, the independent variation of the strides between each body side (decoupling of the sides) allows these animals to bend their land navigation path [35].

Based on the aforementioned aspects, the proposed CPG network considers a tripod pattern at every moment, gait speed variation (the frequency of the entire group of oscillators), and decoupling of the sides.

Figure 9 shows the proposed CPG network architecture where each leg joint is driven by an oscillator represented as a circle. In order to achieve a constant tripod pattern, each CTr joint must have a constant phase angle shift $\theta_{ij} = 90$ deg with respect to the associated TC joint. A 90 deg phase-lag accomplishes a forward walking while a 90 deg phase-lead a backward one.

Furthermore, subsequent TC joints must show a constant phase shift of 180 deg [36]. This synchronization strategy implies a
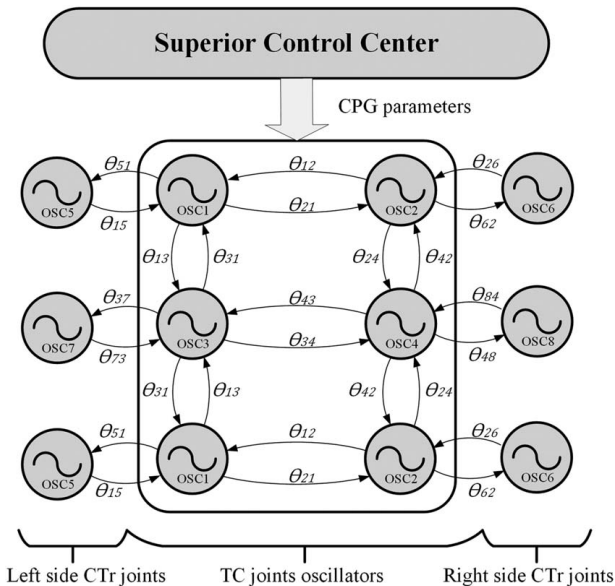

Fig. 9 Network of coupled oscillators

movement in the phase between the front and hind legs of each side of the body. Hence, the same oscillators can be used in these appendices, reducing the total number of needed oscillators from 12 to 8.

The CPG architecture allows modifying the speed and direction of the gait through three parameters: μ, ω, and θ_{ij}. These parameters could be online-driven by superior control centers capable of executing vision, learning, and navigation algorithms.

4 Numerical Simulations

4.1 Numerical Integration of the Central Pattern Generator Equations. The system in Eq. (2) has been numerically solved to obtain a set of reference signals in order to allow the visualization of the network behavior and generate the gait pattern through the actuators.

The numerical integration of Eq. (2) has used a fixed integration step with the Adams method through the Scipy library [37]. This context allows the parameters governing the gait to be modified online for experimental tests. This integration step is limited by the servomotors, which define their angular position by means of a PWM with a period of 20 ms; therefore, the integration step always must be lower than this time value. In addition, the code was compiled into the C language through the Numba library [38], improving the integration time from 3.254 ms to 454×10^{-6} ms. The resulting signals for the four TC joint oscillators after the numerical integration process, with $\varepsilon = 0.3$, $\sqrt{\mu} = 0.9$, $\omega = 0.5$ Hz, and $\theta_{ij} = 180$ deg, are shown in Fig. 10. It can be observed, in steady-state, a phase shift of 180 deg between subsequent TC joints signals, corresponding to 1.0 s, necessary to maintain a tripod gait pattern.

4.2 Central Pattern Generator-Output Space to Joint Space Transformation. The signals generated by the integration of the CPG equations have amplitudes incompatible with the angular range (0–180 deg) of the servomotors. In order to drive the actuators, the amplitudes of the CPG outputs must be mapped to the joint space.

Since the TC joints are driven by oscillators 1–4 (see Fig. 9), let $\varphi_1(t)$ and $\vartheta_1(t) \in \mathbb{R}^4$ be signal vectors in the TC joint space and in the CPG-output space, respectively. Equation (4) provides the relations between the components of these two vectors as expressions mapping the output signals from the CPG-output space (ϑ_{1i}) to the joint space (φ_{1i})

$$\varphi_{1i}(t) = \frac{\sigma}{\sqrt{\mu_{\Delta 1}}} \vartheta_{1i}(t) + \frac{\sigma}{2}, \quad i = 1, 2, 3, 4 \qquad (4)$$

where $\sigma > 0$ is the range of rotation reached by the actuator and $\sqrt{\mu_{\Delta 1}}$ is the maximum amplitude defined for the TC joint CPG oscillators.

For the CTr joints that are driven by oscillators 5–8 (see Fig. 9), let $\varphi_2(t)$ and $\vartheta_2(t) \in \mathbb{R}^4$ be signal vectors in the CTr joint space and in the CPG-output space, respectively. Equation (5), with $i = 1, 2, 3, 4$, transforms the signals from the CPG-output space (ϑ_{2i}) to the joint space (φ_{2i}):

$$\varphi_{2i}(t) = \begin{cases} \dfrac{\sigma}{\sqrt{\mu_{\Delta 2}}} \vartheta_{2i}(t) + \dfrac{\sigma}{2}, & \vartheta_{2i}(t) > 0 \\ \dfrac{\sigma}{2}, & \vartheta_{2i}(t) \leq 0 \end{cases} \qquad (5)$$

where $\sqrt{\mu_{\Delta 2}}$ is the maximum amplitude defined for the CTr joint CPG oscillators.

When applying Eqs. (4) and (5), appropriate reference signals to drive the actuators are obtained. Figure 11 shows the reference signals for a TC amplitude of 50 deg (dashed lines) and a CTr amplitude of 90 deg (continuous lines), corresponding to the joints of the left middle leg for $\sigma = 180$ deg.
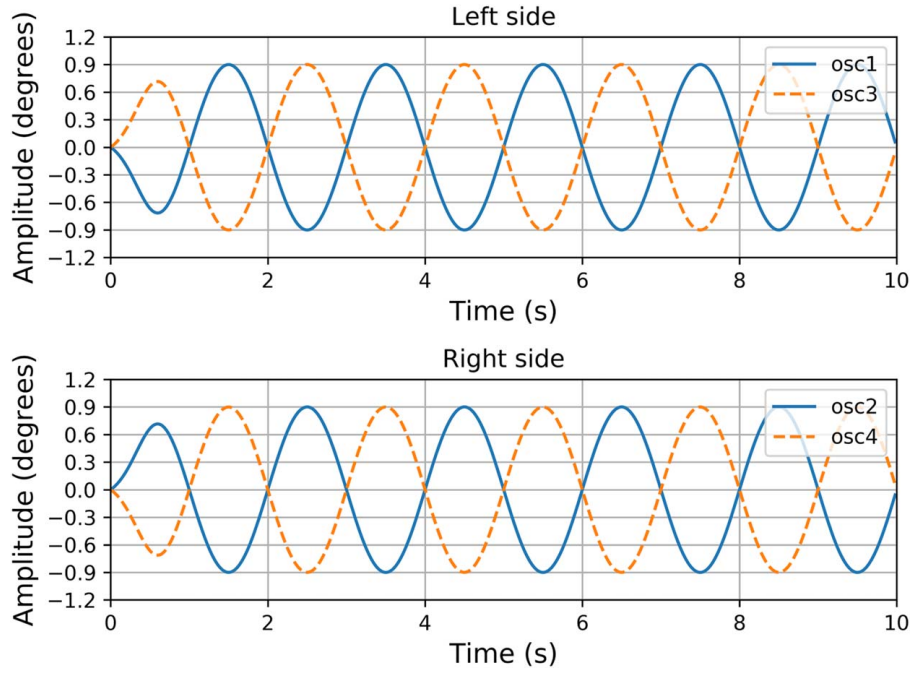
Fig. 10 Outputs of the CPG oscillators for the TC joints

Figure 11 illustrates, in the joint space, sinusoidal behaviors of these signals with their periods of 2 s corresponding to 360 deg. It can be observed, in steady-state, a phase shift of 90 deg corresponding to 0.5 s necessary to maintain a tripod gait pattern.

The gait speed is varied by modifying the oscillation frequency ω of the CPG network. Figure 12 shows the reference signals corresponding to the TC joints of the right and left front legs. The oscillations begin with a frequency of $\pi/2$ Hz (a period of 4 s) and, at $t = 12$ s, they change to π Hz (a period of 2 s). A phase angle of 180 deg between both signals remains constant, so the tripod pattern is not affected.

The independent amplitude variation of the signals that direct the TC joints on each side of the body allows the control of the stride length and, consequently, the gait path direction.

Figure 13 shows independent amplitude variations of the TC joint signals corresponding to the front legs. Both signals have an amplitude of 50 deg in steady-state ($t > 2$ s). At $t = 6$ s, the signal of the right side (dashed lines) reduces its amplitude to 30 deg while the left side (continuous lines) remains invariant and,

finally, at $t = 12$ s, the signal of the left side equals that of the right side. These two changes have been induced.

5 Experimental Results

5.1 Central Pattern Generator Implementation in the Experimental Platform. The integration and mapping scripts of the reference signals are executed in the Raspberry Pi board. These signals are sent via the I2C bus to the PCA9685 board with an average transmission time of 12.65 ms at 400 MHz. Although a 13.104 ms combined average time of the calculation and transmission processes is lower than 20 ms (see Sec. 4), both processes have been executed in parallel to take advantage of the processor resources, measure the execution time, and manage possible failures.

Parallel execution has been achieved by considering each process as a ROS node [30]. To do this, the integration and mapping scripts have been established as a publisher node (sending information)
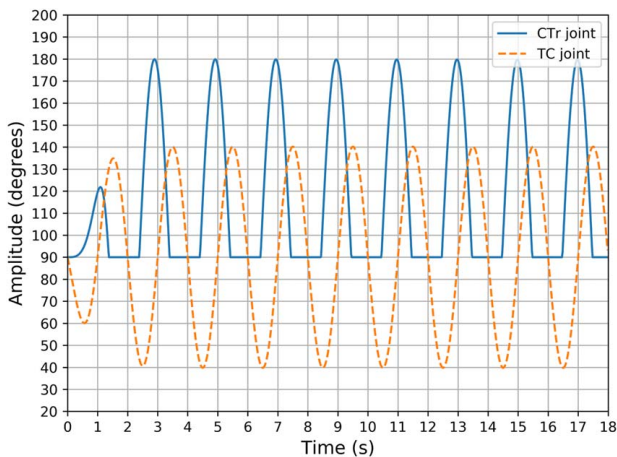

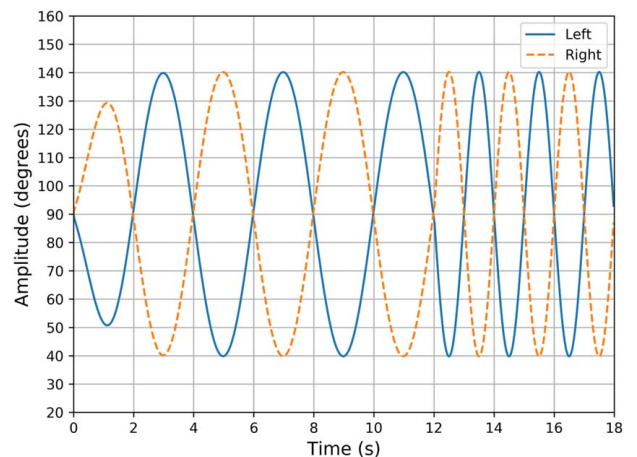**Fig. 11 Synchronization for the CTr and TC joints (left middle leg)**

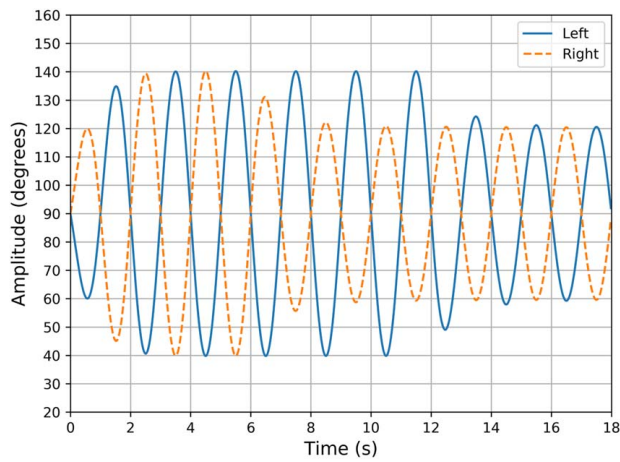**Fig. 12 Frequency transition of the gait for the TC joints**

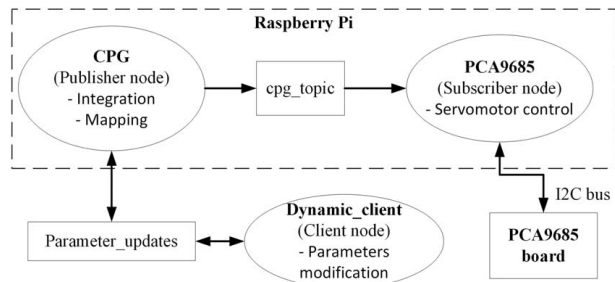**Fig. 13 Amplitude variations for the TC joints (front legs)**

Fig. 14 Node connections for the ROS node graph

while the transmission to the PCA9685 board has been established as a subscriber node (receiving information). The use of ROS nodes allows the amplitude and frequency parameters controlling the gait process to be online-modified from another dynamic client node (modifying parameters). This node could run in a remote computer or in the processor of the robot. Figure 14 illustrates the node connection in a ROS node graph.

A development based on ROS opens the possibility of using its simulation, navigation, and learning tools for future research of the work reported in this paper.

5.2 Measurements of Actuators' Angular Positions. To corroborate the operation of the reference signals, these were compared with the data obtained from the robot joints. These measurements correspond to the angular positions of the servomotors anchored to the joints of the legs when they are excited by the signals calculated in the processor.

Experimental tests were carried out by mounting linear potentiometers directly to the robot joints. These potentiometers were conditioned to vary their output voltage in a range of ±12 V and were clamped to provide a zero potential difference when the servomotors were positioned at 90 deg. Initially, experimental tests were carried out without load (legs in the air). These tests showed negligible errors, i.e., showing almost ideal results. When the robot was placed on rough terrain, under its own weight, the measured signals showed distortions. Linear proportionality was applied to convert volts to degrees in order to perform the aforementioned comparisons.

Since the contralateral front, middle, and hind pairs of legs present similar relative behavior, only the measurement of a single pair was performed. The experimental measurement process is limited by the joint friction that generates vibrations at stride frequencies greater than 0.7 Hz. Furthermore, the potentiometers anchorage the structure, which, being provisionally mounted during the measurement process, is susceptible to misalignment due to rapid movements. In order to avoid mismatches in the measurement system, experiments were carried out taking a maximum step frequency of 0.5 Hz.

Measurements on the frontal TC joints were performed in order to observe variations of stride frequency driven by reference signals generated by the CPG. The reference signals (dashed lines) and their experimental measures (continuous lines) are shown in Fig. 15. The data acquisition begins with a stride frequency of 0.33 Hz, then at $t = 12$ s, it increases to 0.5 Hz and finally it decreases to 0.25 Hz at $t = 20$ s. The physical response of the system gait to the aforementioned frequency variations can be observed in Video S1 (see Video 1 available in the Supplementary Material on the ASME Digital Collection).
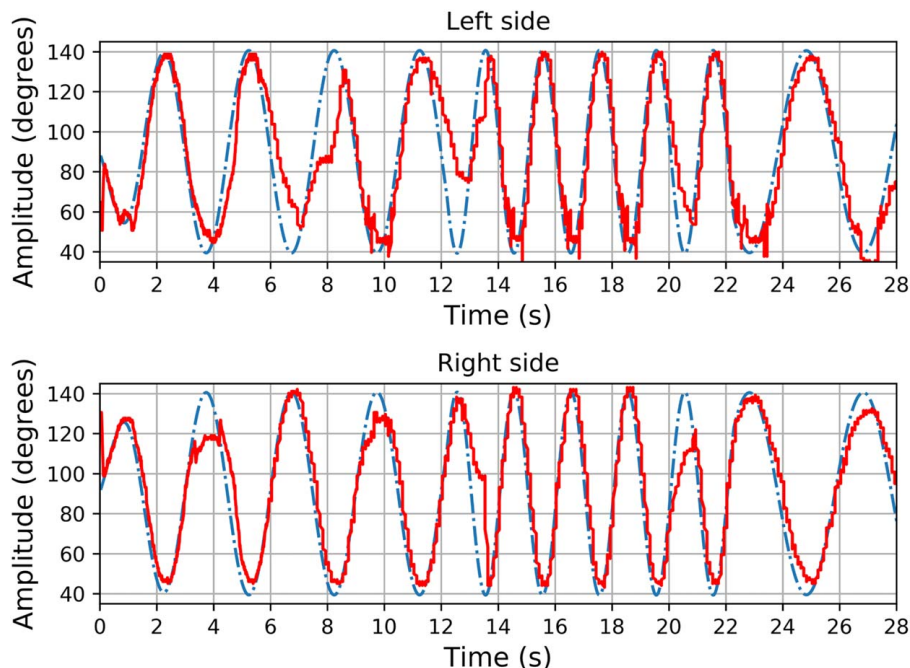

Fig. 15 Frequency transition of the gait trough CPG frequency variation
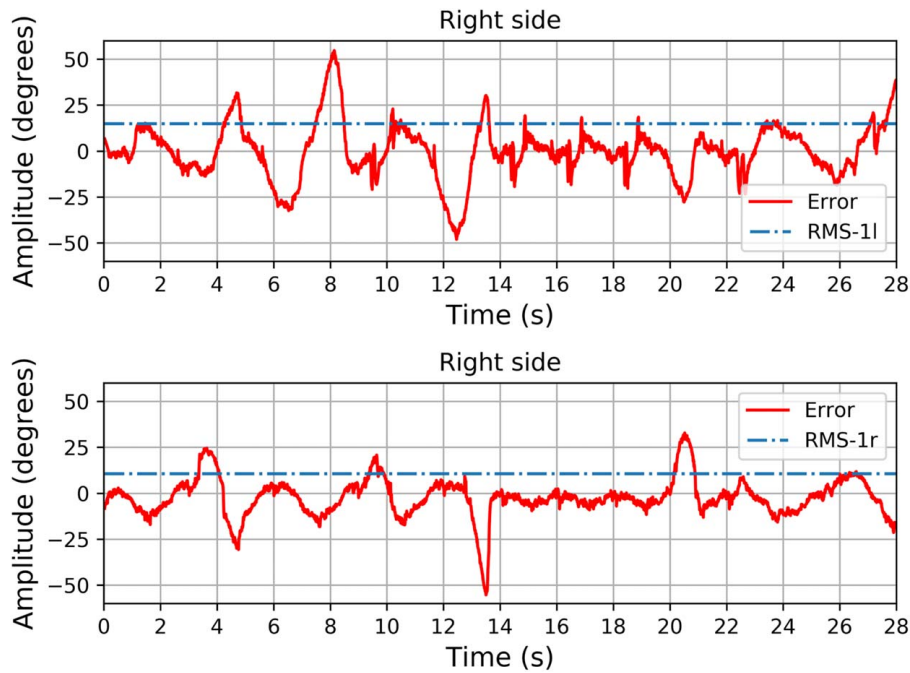
Fig. 16 Errors behavior for frontal TC joints

The experimental measures diverge from the reference signals in three different aspects: lag caused by the response time of the actuators, the presence of noise due to the vibration of the mechanical structures, and deformations induced by the contact of the legs with the floor irregularities. In Fig. 15, it is observed a lower difference between the reference and the measured signals that is inversely proportional to the respective frequency. Figure 16 shows the associated instant error (continuous lines) and the root mean square (RMS) value (dashed line) of this error ($e_{RMS-1l} = 14.91$ deg and $e_{RMS-1r} = 10.61$ deg). It can be noticed that the error tends to an increase in crests and troughs since, at these points, the measured

leg makes contact with the ground or its respective angle rises to its maximum value.

Decoupling of the sides was also measured. Figure 17 shows the experimental responses (continuous lines) of both frontal TC joints to amplitude variations in the reference signals (dashed lines). In steady-state, both joints have amplitudes of 50 deg performing a straight-line walking; at $t = 9$ s, the amplitude of the left side decreases to 20 deg inducing a left-turning gait; and finally, at $t = 20$ s, a right-turning gait is achieved decreasing to 20 deg the right TC joint while returning the left TC joint to its original amplitude. The physical response of the system gait to the
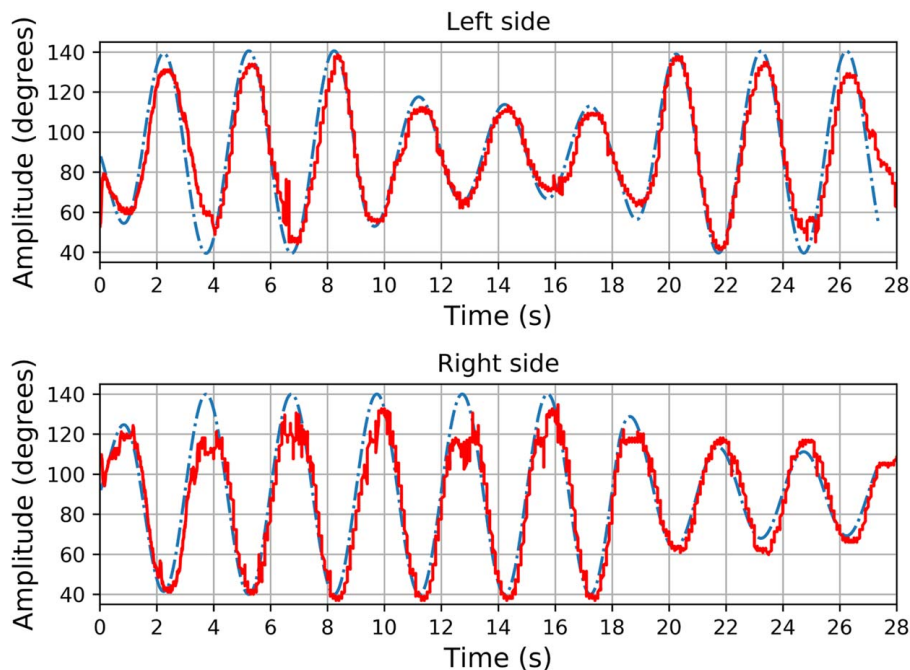

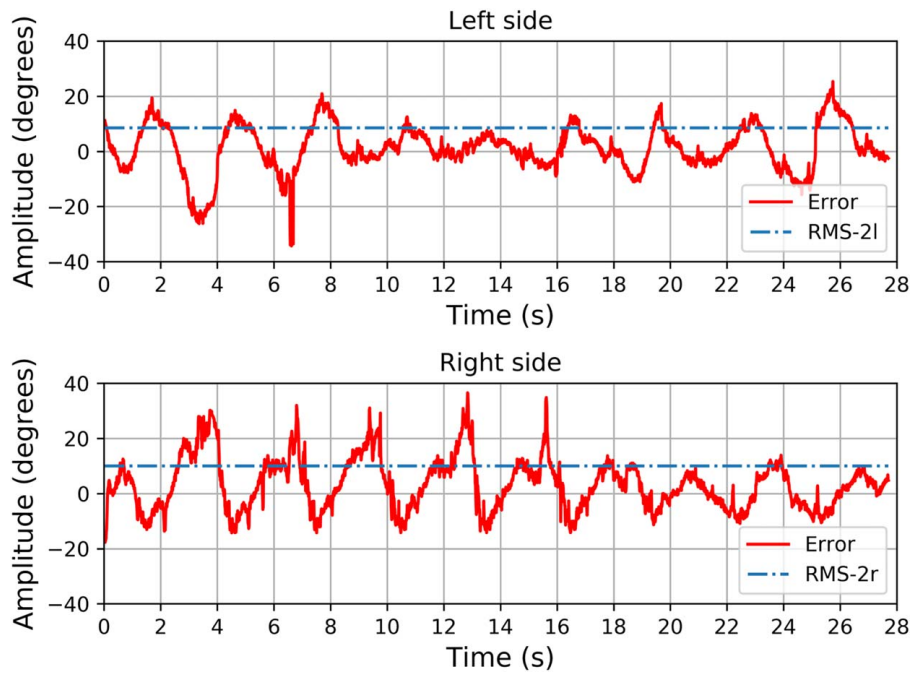**Fig. 17 Measurements of the decoupled amplitude of TC frontal joints**

Fig. 18 Errors behavior for frontal TC joints

aforementioned sides decoupled amplitude variations can be observed in video-2 (see Video 2 available in the Supplementary Material on the ASME Digital Collection).

Similar to the first experiment, the acquired data presented in Fig. 17 exhibit lag, noise, and deformations. Figure 18 shows the instant error between the measured data and the reference signal (continuous lines) as well as the RMS value (dashed lines) of this error ($e_{\text{RMS}-2l} = 8.51$ deg and $e_{\text{RMS}-2r} = 10.01$ deg). In a similar way than in the first experiment, this error is greater in crests and troughs, while it tends to a decrease in inverse proportion to the amplitude.

The relative phase shift between TC and CTr joints has been quantified in order to verify its influence in gait direction.

Figure 19 shows the data obtained from the right frontal leg (continuous lines) when it is excited by reference signals (dashed lines). Figure 19 begins by showing the signals with periods of 3 s corresponding to 360 deg and the CTr joint lagged approximately 0.75 s, corresponding to 90 deg, with respect to the TC joint and, therefore, generating a forward walking. At $t = 10$ s, the signal of the CTr joint gets ahead 0.75 s achieving a backward walking and finally at $t = 20$ s, this signal returns to its original phase shift value. The physical response of the systems gait to the aforementioned relative phase shift variations can be observed in video-3 (see Video 3 available in the Supplementary Material on the ASME Digital Collection).

Figure 20 shows the instantaneous error (continuous lines) and the RMS value (dashed lines) of this error ($e_{\text{RMS}-tc} = 8.52$ deg
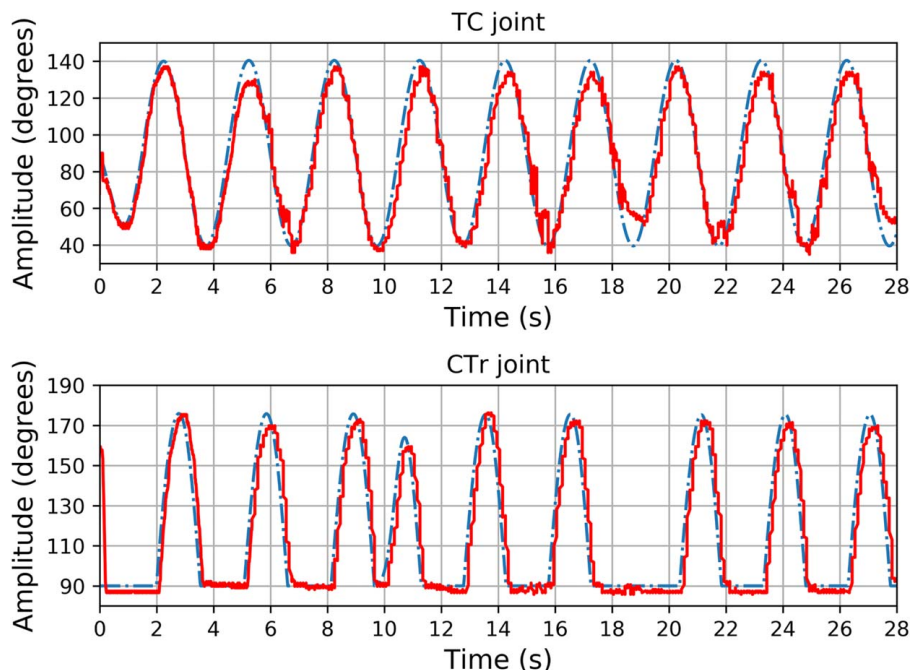

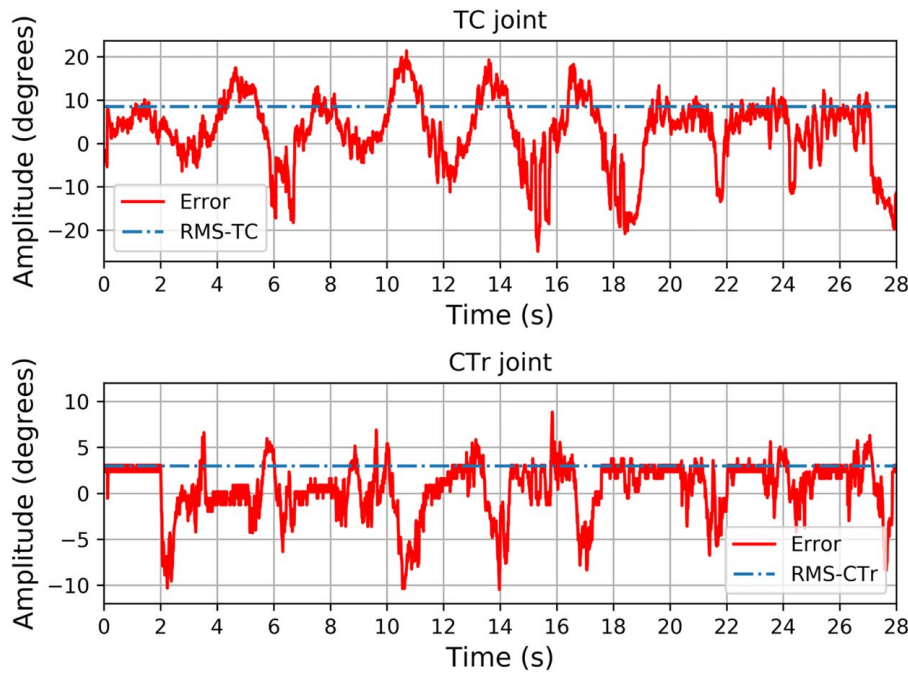**Fig. 19 Phase shift of the CTr joint relative to the TC joint**

Fig. 20 Errors behavior for frontal TC and CTr joints

and $e_{RMS-ctr} = 2.97$ deg) for the front TC and CTr joints. Since the CTr joint holds a lower load than the TC one, it presents an error of smaller amplitude.

The previously referenced videos illustrate the behavior of the walking of the system when it is excited by signals with a frequency low enough to allow the visual observation of this motion. A regular speed gait pattern is shown in video-4 (see Video 4 available in the Supplementary Material on the ASME Digital Collection) where the robot has a stride frequency of 1.25 Hz and a translation speed of 0.2 m/s.

6 Discussion

The online numerical integration (point-by-point) of the coupled oscillators to generate reference signals for the actuators allows modifying the parameters that govern the amplitude, frequency, and relative phase of the hexapod legs at any time.

Potentiometers coupled at the robot joints are allowed to compare experimental data obtained during the walking process with the reference signals generated by the CPG and calculate the error between both signals. Detected deviations such as lag, noise, and deformations induced by the behavior of the actuators do not restrict the general gait process.

Some systems that integrate terrestrial and aerial locomotion from a strongly additive approach, which were introduced in Sec. 1 [10–12] have demonstrated the feasibility of developing aero-terrestrial robotic systems with a morphology of a hexapod with propellers. These works, as the system introduced in this paper, share characteristics such as rotors directly attached to the legs, manufacturing through a 3D printing process and several DoF in the leg with the aim of expanding their mobility. However, the system proposed in this research has advantageous qualities both in its physical structure and in its locomotion algorithm, as it is highlighted below.

The use of only two actuators in combination with a four-bar mechanism per leg reduces the system weight (2100 g) and complexity by decreasing the total DoF of the hexapod from 18 to 12 without affecting the overall walking process. In addition, this mechanism ensures its parallelism with respect to the ground, avoiding the need to adopt rigid postures to start the flight, as it

has been reported in Refs. [10–12]. These postures could interfere with the walking process.

The versatility to modify the speed and direction of the system walking at any time due to the CPG results in an advantage over other similar works that use the inverse kinematics approach. This advantage comes from a network of only eight oscillators inspired by the nervous system of insects, which is simple enough to run in a low-cost embedded electronic system. Better results could be obtained by replacing the current servomotors with others capable of feedback their states, allow the modification of their control law, and have a lighter structure.

7 Conclusions and Future Work

In this paper, the proposal of a novel bioinspired robotic airground system and the strategy for its terrestrial locomotion, based on nonlinear oscillators, have been addressed. The proposed system has, with respect to other works, less weight and complexity and is intended to take off at any time and in any position. Another advantage is the possibility to change, online, the walking pattern of the system by modifying only three gait parameters.

The electronic architecture of the device reported in this paper allows the communication between the embedded microprocessor and a remote terminal using the ROS application. This characteristic grants the possibility to work with more complex algorithms distributed in several computers. Then, robotic collaborative strategies and terrestrial-aerial locomotion could be performed in a relatively simple way.

A versatile terrestrial locomotion, for the bioinspired robot reported in this paper, was achieved based on an eight Hopf oscillator network providing the reference signals that were tracked by the servomotors anchored to the legs. Even when the joints of the robot legs experience errors, these values do not limit nor interfere with the system gait process.

The terrestrial locomotion of the proposed device has been validated by experimental tests, highlighting the possibility of the system to move forward or backward while varying, online, its speed and curving its trajectory.

The generation of gait patterns based on nonlinear oscillator networks for systems of similar morphology but with greater mass is possible if actuators with a higher load capacity are considered.

The tripod walk pattern, being statically stable, is independent of the mass of the system since it does not require a dynamic control system to support the system.

A bigger system with a longer body and legs is also possible. An advantage of the coupled oscillator approach over the traditional inverse kinematics scheme is that it is formulated directly in the joint space and independently of the Cartesian space. This implies that the articular paths of each joint are obtained regardless of the length of the links that constitute the legs.

Future work of this research considers the aerial locomotion of the system in order to establish strategies that take advantage of the aforementioned qualities of the robotic system. The flight process and the transition between terrestrial and aerial modes of locomotion will be the direction for future work, as well as the development of vision and learning algorithms that act as superior control centers in obstacle evasion tasks, the transition between modes of locomotion and autonomous navigation.

Acknowledgment

Data Availability Statement

The datasets generated and supporting the findings of this article are obtainable from the corresponding author upon reasonable request. Data provided by a third party listed in Acknowledgement.

References

[1] Lock, R. J., Burgess, S. C., and Vaidyanathan, R., 2014, "Multi-Modal Locomotion: From Animal to Application," Bioinspir. Biomim., 9(1), pp. 1–18.

[2] Nie, C., Pacheco Corcho, X., and Spenko, M., 2013, "Robots on the Move: Versatility and Complexity in Mobile Robot Locomotion," IEEE Robot. Autom. Mag., 20(4), pp. 72–82.

[3] Sitti, M., Menciassi, A., and Ijspeert, A. J., 2013, "Survey and Introduction to the Focused Section on Bio-Inspired Mechatronics," IEEE/ASME Trans. Mechatron., 18(2), pp. 409–418.

[4] Daler, L., 2015, Ph.D. dissertation, École Polytechnique Fédérale De Lausanne, Lausanne, Switzerland.

[5] Daler, L., Lecoeur, J., Hahlen, P. B., and Floreano, D., 2013, "A Flying Robot With Adaptive Morphology for Multi-Modal Locomotion," IEEE International Conference on Intelligent Robots and Systems, Tokyo, Japan, Nov. 3–7, pp. 1361–1366.

[6] Dudley, C. J., Woods, A. C., and Leang, K. K., 2015, "A Micro Spherical Rolling and Flying Robot," IEEE International Conference on Intelligent Robots and Systems, Hamburg, Germany, Dec., pp. 5863–5869.

[7] Pratt, C. J., and Leang, K. K., 2016, "Dynamic Underactuated Flying-Walking (DUCK) Robot," Proceedings—IEEE International Conference on Robotics and Automation, Stockholm, Sweden, June, pp. 3267–3274.

[8] Araki, B., Koh, J., Guerrero, L., Aukes, D. M., Makineni, A., Tolley, M. T., Rus, D. L., Wood, R. J., Kumar, V., Flying, T., Mulgaonkar, Y., Araki, B., Koh, J., Guerrero-bonilla, L., and Aukes, D. M., 2016, "The Flying Monkey: A Mesoscale Robot That Can Run, Fly, and Grasp," 2016 IEEE International Conference on Robotics and Automation (ICRA), Stockholm, May 16–21, pp. 4672–4679.

[9] Kalantari, A., and Spenko, M., 2012, "Design and Prototyping of a Walking Quadrotor," Proceedings of the ASME Design Engineering Technical Conference, Vol 4 (Parts A and B), Chicago, IL, Aug. 12–15, pp. 1067–1072.

[10] Ratsamee, P., Kriengkomol, P., Arai, T., Kamiyama, K., Mae, Y., Kiyokawa, K., Mashita, T., Uranishi, Y., and Takemura, H., 2016, "A Hybrid Flying and Walking Robot For Steel Bridge Inspection," SSRR 2016—International Symposium on Safety, Security and Rescue Robotics, Lausanne, Switzerland, Oct. 23–27, pp. 62–67.

[11] Pitonyak, M., and Sahin, F., 2017, "A Novel Hexapod Robot Design With Flight Capability," 2017 12th System of Systems Engineering Conference, SoSE, Waikoloa, USA, June 18–21, pp. 1–6.

[12] Pitonyak, M., and Sahin, F., 2017, "Locomotion and Transitional Procedures for a Hexapod-Quadcopter Robot," 2017 IEEE International Conference on Systems, Man, and Cybernetics, SMC 2017, Alberta, Canada, Oct. 5–8, pp. 1447–1452.

[13] Peterson, K., and Fearing, R. S., 2011, "Experimental Dynamics of Wing Assisted Running for a Bipedal Ornithopter," IEEE International Conference on Intelligent Robots and Systems, San Francisco, CA, Sept. 25–30, pp. 5080–5086.

[14] Woodward, M. A., and Sitti, M., 2014, "MultiMo-Bat: A Biologically Inspired Integrated Jumping-Gliding Robot," Int. J. Robot. Res., 33(12), pp. 1511–1529.

[15] Bruzzone, L., and Quaglia, G., 2012, "Review Article: Locomotion Systems for Ground Mobile Robots in Unstructured Environments," Mech. Sci., 3(2), pp. 49–62.

[16] Mintchev, S., and Floreano, D., 2016, "Adaptive Morphology: A Design Principle for Multimodal and Multifunctional Robots," IEEE Robot. Automat. Mag., 23(3), pp. 42–54.

[17] RunBin, C., YangZheng, C., Lin, L., Jian, W., and Xu, M. H., 2013, "Inverse Kinematics of a New Quadruped Robot Control Method," Int. J. Adv. Robot. Syst., 10(1), p. 46.

[18] Park, H., Kwak, B., and Bae, J., 2018, "Inverse Kinematics Analysis and COG Trajectory Planning Algorithms for Stable Walking of a Quadruped Robot With Redundant DOFs," J. Bionic Eng., 15(4), pp. 610–622.

[19] Mulloney, B., and Smarandache, C., 2010, "Fifty Years of CPGs: Two Neuroethological Papers That Shaped the Course of Neuroscience," Front. Behav. Neurosci., 4(45), pp. 1–8.

[20] Hughes, G. M., and Wiersma, C. A. G., 1960, "The Co-ordination of Swimmeret Movements in the Crayfish, Procambarus Clarkii (Girard)," J. Exp. Biol., 37(4), pp. 657–670.

[21] Ijspeert, A. J., 2008, "Central Pattern Generators for Locomotion Control in Animals and Robots: A Review," Neural Netw., 21(4), pp. 642–653.

[22] Ding, R., Yu, J., Yang, Q., and Tan, M., 2013, "Dynamic Modelling of a CPG-Controlled Amphibious Biomimetic Swimming Robot," Int. J. Adv. Robot. Syst., 10(4), p. 199.

[23] Suzuki, H., Lee, J. H., and Okamoto, S., 2017, "Development of Semi-Passive Biped Walking Robot Embedded With CPG-Based Locomotion Control," 2017 14th International Conference on Ubiquitous Robots and Ambient Intelligence, URAI, Jeju, South Korea, June 28–July 1, pp. 75–78.

[24] Zhang, J., Gao, F., Han, X., Chen, X., and Han, X., 2014, "Trot Gait Design and CPG Method for a Quadruped Robot," J. Bionic Eng., 11(1), pp. 18–25.

[25] Fang, Y., Hu, J., Liu, W., Chen, B., Qi, J., and Ye, X., 2016, "A CPG-Based Online Trajectory Planning Method for Industrial Manipulators," Proceedings of 2016 Asia-Pacific Conference on Intelligent Robot Systems, ACIRS 2016, Tokyo, Japan, July 20–22, pp. 41–46.

[26] Fang, Y., Hu, J., Qi, J., Liu, W., Wang, W., and Peng, Y., 2019, "Planning Trigonometric Frequency Central Pattern Generator Trajectory for Cyclic Tasks of Robot Manipulators," Proc. Inst. Mech. Eng. C, 233(11), pp. 4014–4031.

[27] Tian, J., and Lu, Q., 2015, "Simulation of Octopus Arm Based on Coupled CPGs," J. Robot., 2015(3), pp. 1–9.

[28] Guo, X., Chen, L., Zhang, Y., Yang, P., and Zhang, L., 2010, "A Study on Control Mechanism of Above Knee Robotic Prosthesis Based on CPG Model," 2010 IEEE International Conference on Robotics and Biomimetics, ROBIO, Tianjin, China, Dec. 14–18, pp. 283–287.

[29] Steingrube, S., Timme, M., Wörgötter, F., and Manoonpong, P., 2010, "Self-Organized Adaptation of a Simple Neural Circuit Enables Complex Robot Behaviour," Nat. Phys., 6(3), pp. 224–230.

[30] Quigley, M., Gerkey, B., Conley, K., Faust, J., Foote, T., Leibs, J., Berger, E., Wheeler, R., and Ng, A., 2009, "ROS: An Open-Source Robot Operating System," International Conference on Robotics and Automation (ICRA), Kobe, Japan, May 12–17, pp. 1–5.

[31] Mees, A. I., and Chua, L. O., 1979, "The Hopf Bifurcation Theorem and Its Applications to Nonlinear Oscillations in Circuits and Systems," IEEE Trans. Circuits Syst., 26(4), pp. 235–254.

[32] Oh, C. H., and Singh, K., 1994, "Generalized Q-Oscillators and Their Hopf Structures," J. Phys. A: Math. Gen., 27(17), pp. 5907–5918.

[33] Lauter, R., Brendel, C., Habraken, S. J. M., and Marquardt, F., 2015, "Pattern Phase Diagram for Two-Dimensional Arrays of Coupled Limit-Cycle Oscillators," Phys. Rev. E: Stat., Nonlinear, Soft Matter Phys., 92(1), pp. 1–8.

[34] Zhou, C., and Low, K. H., 2012, "Design and Locomotion Control of a Biomimetic Underwater Vehicle With Fin Propulsion," IEEE/ASME Trans. Mechatron., 17(1), pp. 25–35.

[35] Zollikofer, C. P. E., 1994, "Stepping Patterns in Ants," J. Exp. Biol., 192(1), pp. 119–127.

[36] Wilson, D. M., 1966, "Insect Walking," Annu. Rev. Entomol., 11(1), pp. 103–122.

[37] Vijaykumar, A., Bardelli, P., Rothberg, A., Hilboll, A., Kloeckner, A., Scopatz, A., Lee, L., Rokem, A., Woods, C. N., Fulton, C., Masson, C., Häggström, C., Fitzgerald, C., Nicholson, D. A., Hagen, D. R., Pasechnik, D. V., Olivetti, E., Martin, Wieser, E., Silva, F., Lenders, F., Wilhelm, F., Young, G., Price, G. A., Ingold, G. L., Allen, G. E., Lee, G. R., Audren, H., Probst, I., Dietrich, J. P., Silterra, J., Webber, J. T., Slavič, J., Nothman, J., Buchner, J., Kulick, J., Schönberger, J. L., de Miranda Cardoso, J. V., Reimer, J., Harrington, J., Cano Rodríguez, J. L., Nunez-Iglesias, J., Kuczynski, J., Tritz, K., Thoma, M., Newville, M., Kümmerer, M., Bolingbroke, M., Tartre, M., Pak, M., Smith, N. J., Nowaczyk, N., Shebanov, N., Pavlyk, O., Brodtkorb, P. A., Lee, P., McGibbon, R. T., Feldbauer, R., Lewis, S., Tygier, S., Sievert, S., Vigna, S., Peterson, S., More, S., Pudlik, T., Oshima, T., Pingel, T. J., Robitaille, T. P., Spura, T., Jones, T. R., Cera, T., Leslie, T., Zito, T., Krauss, T., Upadhyay, U., Halchenko, Y. O., and Vázquez-Baeza, Y., 2020, "SciPy 1.0: Fundamental Algorithms for Scientific Computing in Python," Nature Methods, 17(3), pp. 261–272.

[38] Lam, S. K., Pitrou, A., and Seibert, S., 2015, "Numba: A LLVM-Based Python JIT Compiler," Proceedings of the Second Workshop on the LLVM Compiler Infrastructure in HPC, Austin, TX, Nov., pp. 1–6.